A representative volume element model for ultra-high-molecular-weight-polyethylene composites

D. Kempesis [a,*], L. Iannucci [a], S. Del Rosso [a], P.T. Curtis [a], D. Pope [b], P.W. Duke [b]

[a] Imperial College London, Exhibition Road, SW7 2AZ London, UK
[b] Defence Science and Technology Laboratory, Porton Down, Salisbury SP4 0JQ, UK

ARTICLE INFO

ABSTRACT

This paper presents the development of a Representative Volume Element (RVE) for Ultra-high-Molecular-Weight-Polyethylene (UHMWPE) composites. The numerical models were based on the fibrillar nature of UHMWPE fibres, which consist of smaller scale, continuous through-the-length macro-fibrils. A three-dimensional constitutive model for UHMWPE macro-fibrils was developed and implemented in the LS-DYNA explicit finite element (FE) code, through a user-defined subroutine. The proposed transversely isotropic model accounts for viscoelastic effects in the principal direction of the fibre coupled with the continuum damage mechanics approach. Energy dissipation associated with failure was controlled through an objectivity algorithm to provide mesh insensitive solutions. Hill's yield criterion was used to capture the non-linear response of the fibre in the transverse direction. The RVE was built from macro-fibrils and a Thermoplastic Polyurethane (TPU) resin in order to study the micromechanical response of the polymeric composite laminate. Periodic boundary conditions (PBC) were imposed in the model and a penalty-based cohesive contact algorithm was used to simulate interfibrillar interactions and the interface between the macro-fibrils and the resin. The proposed RVE model provides insight on microscale deformation mechanisms in UHMWPE composites under different loading conditions.

1. Introduction

Improving combat survivability has always been a crucial task in military technology. Composite materials are being used in ballistic protection systems due to their combination of high strength and low density. One of the most promising materials is the UHMWPE fibre-reinforced composite, Dyneema® HB26, that has shown excellent projectile capturing capabilities and can be used in both military and civil applications. The aforementioned composite consists of Dyneema® SK76 filaments and an optimised polyetherdiol-aliphatic diisocyanate polyurethane (PADP) resin.

Dyneema® SK76 filament's microstructure is very similar to the one of SK75. In the work of Marissen [1], when the fibre was stretched over a sharp razor, it revealed its fibrillar nature. Strawhecker et al. [2], used an Atomic Force Microscope (AFM) to examine the surface of UHMWPE single filaments which failed across a shear plane. The observed morphology consisted of smaller scale structures (micro-fibrils), bundles of fibrils (macro-fibrils), amorphous material and voids. From references [1,2], it can be safely assumed that macro-

fibrils are continuous through the length of the filament. The tensile response of Dyneema® SK76 single filaments has been studied by various researchers [3–5] and showed dependency on the loading rate. Under transverse compression UHMWPE fibres revealed geometrical (fibrillation) and material (plasticity) non-linearities [6]. A macro-fibril based numerical model for the fibre and a macro-fibril constitutive model are proposed in this study to describe the mechanical behaviour and through-thickness deformation of the fibre.

Current and past trends in RVE modelling [7–9] tend to treat the fibres as a homogenised continuum. While this method provides useful insight on the laminate's micromechanical behaviour, the hierarchical morphology of polymeric fibres could affect the deformation and contribute to the overall non-linearity of the composite material. In the scope of this work, the microstructure of the fibre has been explicitly implemented to provide an extra layer of numerical fidelity while also allowing the visualisation of stress concentrations, detailed strain-fields and potential fibrillation evolution.

The proposed macro-fibril based fibre model was used to develop a RVE for the Dyneema® HB26 laminates. The volume fraction (V_f) of

the laminate can be as high as 83% leading to a resin starved configuration [3,10]. These laminates are produced with a [0/90]n lay-up where each layer has effectively four fibres through-the-thickness very closely packed together, leaving very little space for the resin. The laminate inherits the properties of both the fibres and the resin, which makes it strain-rate dependent, with elasto-viscoplastic behaviour in the out-of-plane directions and under shear [3,10–12]. The RVE is expected to be a powerful numerical tool to help identify and tailor the most important parameters that affect the mechanical behaviour of the material. Furthermore, this micromechanical analysis can be used in an inverse manner to optimise the ply and the laminate based on the desired application.

2. Constitutive model

The proposed constitutive model was based on an incremental Lagrangian formulation, which is used in LS-DYNA explicit FE codes for 3D solid brick elements [13]. The mathematical expressions presented in this section were used to describe the behaviour of a transversely isotropic UHMWPE macro-fibril.

2.1. Coupled viscoelastic-damage constitutive behaviour

A generalised Maxwell model with six elements was used to simulate viscoelastic effects in the longitudinal direction of the macro-fibril. Stress can be calculated using the Boltzman integral:

$$\sigma(t) = \int_0^t E(t - \tau)\dot{\varepsilon}(\tau)d\tau \tag{1}$$

where σ is the value of stress at current time t, E is the elastic modulus, τ is a variable introduced to account for the stress history of the material, and $\dot{\varepsilon}$ the strain rate. Relaxation of the elastic modulus over time can be expressed in terms of Prony series:

$$E(t) = E_0\left[1 - \sum_{i=1}^6 p_i\left(1 - e^{\frac{-t}{\tau_i}}\right)\right] \tag{2}$$

where E_0 is the instantaneous modulus of the material, p_i and τ_i are the ith Prony series constant and retardation time respectively [14]. Failure initiation in the longitudinal direction of the macro-fibril was predicted using the maximum stress criterion:

$$\text{FI} = \frac{\sigma_{11}^{n+1}}{X_T} \tag{3}$$

where FI the failure index associated with tensile failure initiation, σ_{11}^{n+1} is the stress in the longitudinal direction at a time step $n + 1$ and X_T is the tensile strength of a macro-fibril. A linear unloading regime was assumed in the damage evolution region. The damage evolution equation can be defined as:

$$d_1 = \frac{\varepsilon_{f,11}}{(\varepsilon_{f,11} - \varepsilon_{0,11})}\left(1 - \frac{\varepsilon_{0,11}}{\varepsilon_{11}}\right) \tag{4}$$

where d_1 is the total damage in 11-direction of the material, $\varepsilon_{0,11}$ is the strain where damage initiates in the 11-direction and $\varepsilon_{f,11}$ is the strain to failure where the material has lost its ability to carry any loading. For the implementation in the FE code, damage should be given in an incremental form as follows:

$$\Delta d_1 = \frac{\varepsilon_{f,11}}{(\varepsilon_{f,11} - \varepsilon_{0,11})}\left(\frac{\varepsilon_{0,11}}{\varepsilon_{11}^2}\right)\Delta\varepsilon_{11} \tag{5}$$

$$d_1^{n+1} = d_1^n + \Delta d_1 \tag{6}$$

where Δd_1 is the damage increase for a strain increment $\Delta\varepsilon_{11}$. Damage starts to develop when the failure index reaches the value of one and it is considered irreversible. The Poisson's ratio must be reduced accordingly in order to maintain a positive definite solution.

$$\nu_{12} = \nu_{12}\left(1 - d_1^{n+1}\right) \tag{7}$$

$$\nu_{13} = \nu_{13}\left(1 - d_1^{n+1}\right) \tag{8}$$

2.2. Plasticity

Experimental studies on single fibre, through-thickness compression, have reported a non-linear stress–strain behaviour with large inelastic strain being present [6]. The plastic behaviour of the fibre was simulated by the Hill's yield criterion where the yield function can be expressed as:

$$\Phi = F_1(\sigma_{11} - \sigma_{22})^2 + F_2(\sigma_{22} - \sigma_{33})^2 + F_3(\sigma_{33} - \sigma_{11})^2 + F_4\sigma_{12}^2$$
$$+ F_5\sigma_{23}^2 + F_6\sigma_{13}^2$$
$$= \bar{\sigma}^2 \tag{9}$$

where F_i are constants related to the yield stress and $\bar{\sigma}$ is a function of the yield stress over the accumulated plastic stain which provides the isotropic strain hardening behaviour in the model. The constants can be defined as:

$$
\begin{aligned}
F_1 &= \frac{1}{2}\left(\frac{1}{\sigma_{y,11}^2} + \frac{1}{\sigma_{y,22}^2} - \frac{1}{\sigma_{y,33}^2}\right), \\
F_2 &= \frac{1}{2}\left(\frac{1}{\sigma_{y,22}^2} + \frac{1}{\sigma_{y,33}^2} - \frac{1}{\sigma_{y,11}^2}\right), \\
F_3 &= \frac{1}{2}\left(\frac{1}{\sigma_{y,11}^2} + \frac{1}{\sigma_{y,33}^2} - \frac{1}{\sigma_{y,22}^2}\right), \\
F_4 &= \frac{1}{\sigma_{y,12}^2}, \quad F_5 = \frac{1}{\sigma_{y,23}^2}, \quad F_6 = \frac{1}{\sigma_{y,13}^2}
\end{aligned}
\tag{10}
$$

where $\sigma_{y,ij}$ are the yield stresses in each corresponding direction i,j. Yielding is assumed only in the transverse direction 22 and 33 and under in-plane shear 12. The rate of plastic flow is given by $\dot{\varepsilon}_i^p$ in the following equation:

$$\dot{\varepsilon}_i^p = \dot{\gamma}\frac{\partial\Phi}{\partial\sigma_i} \tag{11}$$

where γ is the non-negative plastic multiplier. The detailed methodology for calculating the plastic multiplier is described in B, following the methodology of de Souza Neto et al. [15].

2.3. Mesh sensitivity

Different element sizes are commonly used in FE models. The internal energy of an element is related to its volume and hence, the dissipated energy, during damage propagation, is going to be different for each element size. In order to avoid mesh dependent solutions and strain localisation problems, a smeared cracking approach, which links damage and fracture mechanics, has been adopted. This approach is based on a representative unit volume where its stored energy should be related to the fracture energy of the material [16,17]. The specific energy dissipated is the area under the stress–strain curve and can be defined as:

$$U_f = \int_0^\infty \sigma_{ij}d\varepsilon_{ij} \tag{12}$$

The total specific energy can be subdivided, as seen in Eq. (13), into elastic (U_e) and viscoelastic (U_{ve}) energy which is stored prior to failure and propagation energy (U_p). A representation of the constitutive law for a unit volume can be seen in Fig. 1.

$$U_f = U_e + U_{ve} + U_p \tag{13}$$

The translaminar fracture energy (Γ_f) is a material property for each mode of failure and can be derived from the following equation:

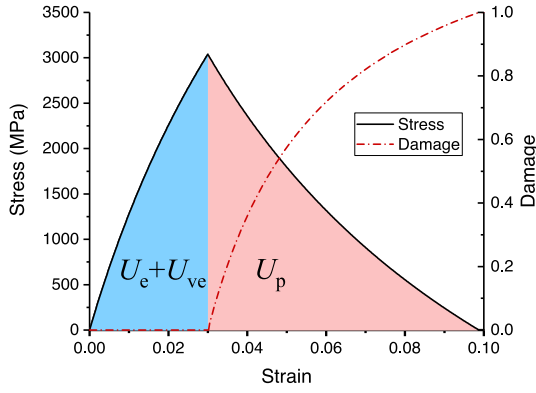$$\Gamma_f = \int_0^\infty \sigma_{ij}d\delta_{ij} \tag{14}$$

Fig. 1. Constitutive law schematic.

The characteristic length (l^*) is a geometric quantity of a finite element which relates the damaged element area with the longest element length in the loading direction.

$$U_f V_e = \Gamma_f A_e \tag{15}$$

$$l^* = A_e / l_1 \tag{16}$$

where l_1 is the longest length of an element with area A_e and V_e is the element volume.

The aforementioned approach has been widely used in other studies but it has the following limitations. Firstly, it applies only to structured meshes which is not the case for most FE models in engineering applications. Complex geometries are often being studied and geometric discontinuities might be present. Secondly, the crack growth direction can only be parallel to one of the element edges, which imposes limitations when models include multi-directional composite laminates, since each layer can have arbitary directions.

In order to overcome the aforementioned limitations of the smeared crack approach, an algorithm was used to calculate the characteristic length of each element and ensure objectivity of the model. This method was based on the Jacobian of the element and it was originally proposed by Oliver [18] for shell elements. Based on the aforementioned work, an extended algorithm for 3D solid elements was proposed by Donadon et al. [19] and it was used in this study. The following equation was used to calculate the element characteristic length in the longitudinal direction.

$$l_{11}^T = \left(\sum_{i=1}^{n_c} \left[\frac{\partial N_i(\xi_j, n_j)}{\partial x} \cos(\theta_f) + \frac{\partial N_i(\xi_j, n_j)}{\partial y} \sin(\theta_f) \right] \theta_i \right)^{-1} \tag{17}$$

where ξ, n the element isoparametric coordinates, n_c is the number of corner nodes in the virtual midplane of the element, N_i the shape functions of the virtual midplane nodes, θ_f the angle of the macro-fibril with respect to the fibre and θ_i a function which can take the values of either 1 or 0 depending on the virtual node position. In case the node is ahead of the crack $\theta_i = 1$, otherwise $\theta_i = 0$. The superscript t refers to the tensile mode of failure where the characteristic length is calculated.

For a linear unloading law after failure initiation, the failure strains for each element can be calculated accordingly incorporating the fracture energy of the material.

$$\varepsilon_{ij}^f = \frac{2}{\sigma_{ij}\left(\varepsilon_{ij}^{max}\right)} \left[\frac{\Gamma_{f_{ij}}^k}{l_{ij}^k} - \int_0^{\varepsilon_{ij}^{max}} \sigma_{ij}(\varepsilon_{ij}) d\varepsilon_{ij} \right] + \varepsilon_{ij}^{max} \tag{18}$$

where $k = T$ for the tensile failure mode and $i = j = 1$ for the longitudinal direction of the fibre. The detailed methodology of the characteristic length calculation is given in [19].

3. Finite element modelling

3.1. Single fibre model

Macro-fibrils in the fibre cross-section need to be explicitly modelled as well as the interactions between them in order to predict geometrical non-linearities observed in experiments. The size of the micro-fibrils in UHMWPE fibres can vary from a few nanometers to a few hundred nanometers, typically from 8 nm to 100 nm. On the other hand, the size of the macro-fibrils can be from 100 nm to 3 μm [20]. Strawhecker et al. [2] measured an average value for the macro-fibril width, which can be used for modelling. For a Dyneema® SK76 fibre with a nominal diameter of 14 μm the measured macro-fibril width was 934 nm. The fibre model was assumed to have a circular cross-section with a diameter of 17 μm. The total number of macro-fibrils in the fibre cross-section was roughly 253 with an average width of 1 μm and were modelled according to a Laguerre-Voronoi tessellation. The microstructure package VorTeX, that was already available in LS-PrePost, was used to generate the cross-section of the fibre, as seen in Fig. 2. A detailed explanation on how the geometry of the tessellation is generated can be found in reference [21].

The smaller scale micro-fibrils behave cohesively with respect to larger sub-groups in the fibre [2]. McDaniel et al. [22], performed peel tests on Dyneema® SK76 single filaments to determine the Mode I and Mode II energy release rates. The peak normal and shear stresses were 5 MPa and 30 MPa and Mode I and Mode II fracture energies 500 J/m² and 3,460 J/m² respectively. Macro-fibril interactions were modelled using a penalty-based cohesive contact logic already available in LS-DYNA, Automatic One-Way Surface to Surface Tiebreak, with option 9 enabled.

In order to minimise the computational cost of the single fibre tensile test simulation, a quarter symmetric model was built with displacement controlled boundary conditions. The tabs of the machine were not modelled for simplicity and the loading was applied directly on the free face of the fibre. Loading conditions were applied as nodal velocities with an S-shaped curve to simulate the loading conditions imposed under actual experimental conditions. The length of the fibre in the FE model was 50 time larger than the radius which resulted in having a total of 13,035 solid brick elements.

To simulate the out-of-plane compressive behaviour of a single fibre, the platens of the machine had to be explicitly modelled and were assumed to be rigid. The Laguerre-Voronoi tessellation resulted in an asymmetric fibre cross section, making the modelling of the
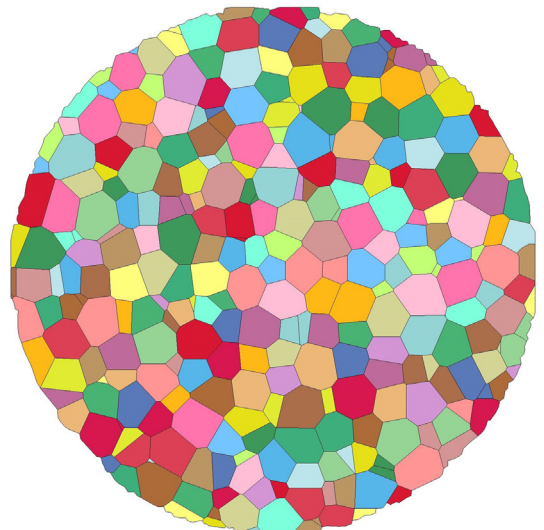

Fig. 2. Dyneema® SK76 cross-section numerical model.

whole fibre cross-section necessary. As indicated in former studies [23,24], the assumption of plane strain conditions is valid when studying the out-of-plane compressive behaviour of a filament. Therefore, only one element was used, with symmetry boundary conditions, in the axial direction of the fibre. The numerical model consisted of 7655 solid elements in the cross section of the fibre and 732 solid elements in the rigid platens.

3.2. RVE model

The Dyneema® HB26 RVE model was developed using macro-fibrils and resin. An image of the 0/90 RVE numerical model is presented in Fig. 3, where the mesh was removed for clarity. The fibres were modelled in a confined configuration in order to achieve a high volume fraction of 80%. A minimum of three elements per face in contact is required to achieve correct energy dissipation in the cohesive zone [23,25], leading to a total of 16,324 solid element for the resin and 133,892 solid elements for the macro-fibrils. The proposed user-defined material model, was used for the macro-fibrils, while a strain-rate dependent elasto-plastic constitutive law was used for the resin. The software Altair HyperMesh™ was used to mesh the model.

Periodic boundary conditions (PBC) were imposed in the RVE model. Control elements were created for each normal direction in order to couple the macroscopic strain to the microscopic perturbed displacements. Nodal displacements of opposing surfaces are coupled according to the equation set in Eq. (19).

$$
\begin{aligned}
u_x|_{x=0} - u_x|_{x=l_x} &= \varepsilon_x l_x + \varepsilon_{xy} l_y + \varepsilon_{xz} l_z \\
u_y|_{y=0} - u_y|_{y=l_y} &= \varepsilon_{xy} l_x + \varepsilon_y l_y + \varepsilon_{yz} l_z \\
u_z|_{z=0} - u_z|_{z=l_z} &= \varepsilon_{xz} l_x + \varepsilon_{yz} l_y + \varepsilon_z l_z
\end{aligned}
\tag{19}
$$

The Constrained Multiple Global option was used to couple opposing nodes in the model. In order to avoid redundancy in the numerical implementation of PBC, nodal sets for the RVE corner nodes, edges and the remaining surfaces were created. A similar approach to the one in the work of Gar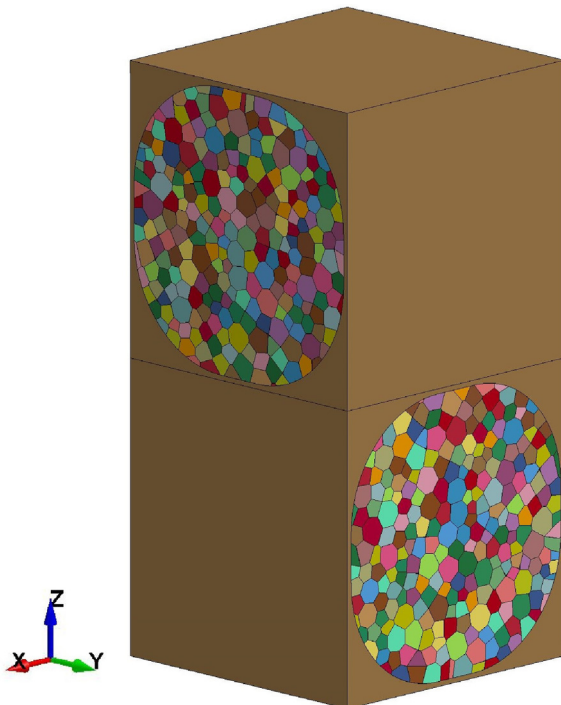oz et al. [26] was followed to impose constraints on the aforementioned sets. A MATLAB® script was developed for the node pair selection and generation of the required keyword input file.

The same penalty-based cohesive contact algorithm that used to model the interactions between macro-fibrils, was also employed to simulate the interfaces between the fibres and the resin as well as the bonding between the 0 and 90 degree layers. For the latter, the interlaminar strength values from the work of Lässig et al. [27] were used, with normal peak and shear stress 1.07 MPa and 2.61 MPa respectively. Fracture energies from the work of Grujicic et al. [28] were selected with Mode I and Mode II having the values of 544.7 J/m^2 and 1460 J/m^2 respectively. Due to lack of single fibre pull-out experimental data, the properties of the macro-fibril cohesive interactions were used to model the interface between the fibres and the resin.

4. Results and numerical model validation

4.1. Mesh sensitivity study

A 20 mm × 10 mm × 1 mm strip was loaded in the longitudinal direction under a quasi-static (0.01/s) displacement controlled tensile fashion. Three different element sizes were tested in order to validate the mesh sensitivity of the constitutive model. A fracture energy of 1500 kJ/m^2 was used for the mesh sensitivity analysis in order to prevent negative values for U_p when using large finite elements. The results can be seen in Fig. 4. The force–displacement curve is identical for various element lengths which shows no mesh dependency.

4.2. Single fibre results

The parameter identification process for the viscoelastic model was done using the LS-OPT optimization software to match the numerical with the experimentally obtained relaxation response of a single fibre. Fibre relaxation tests were performed according to the methodology presented in the work of Del Rosso [29], for a fibre gauge length of 100 mm and a tensile loading rate of 100 mm/min. As seen in Fig. 5, the experimentally obtained relaxation response of a Dyneema® SK76 fibre was predicted with excellent agreement. The predicted tensile response was compared to experimental results as seen in Fig. 6. The parameters used in the macro-fibril constitutive model can be seen in Table 1. Russell et al. [3] reported a reduction in yarn strength associated with the waviness of the fibres. The tensile strength of the fibre could also be affected by the waviness and misalignment of the macro-fibrils. Since none of the above were explicitly modelled, the strength of the single fibre (4 GPa) was used.

Good correlation was observed between the experimental and numerical results for a single fibre under tensile loading conditions,
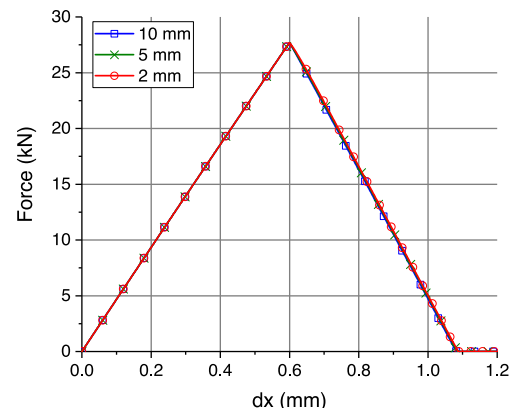

Fig. 3. UHMWPE 0/90 macro-fibril based RVE numerical model.

Fig. 4. Force–displacement relationship for different element sizes.
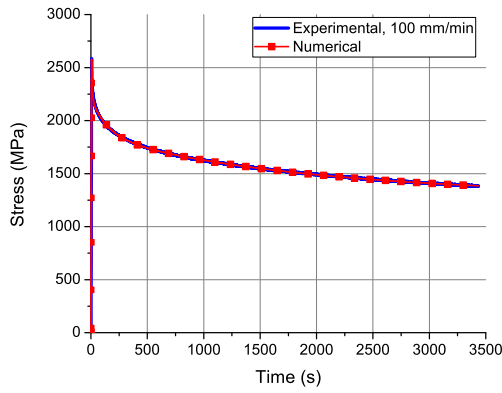
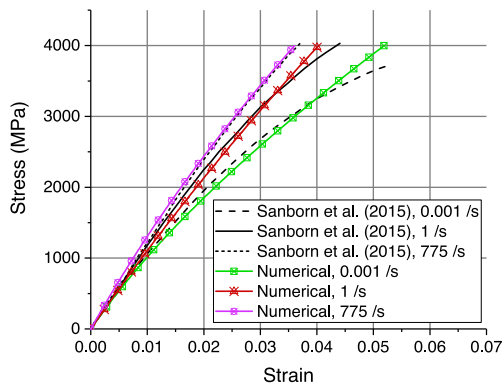Fig. 5. Single fibre experimental and numerical relaxation response.

Fig. 6. Single fibre experimental and numerical tensile response.

with small discrepancies in the non-linearity of the stress–strain curve. Discrepancies in the non-linearity of the slope could be attributed to the load distribution through-the-thickness of the fibre which was not considered in the numerical model, since the grips of the machine were not modelled. However, a direct gripping method was used in the experimental procedure in [5] and no slippage from the grips was observed. Therefore, the additional non-linearity could be attributed to non-linear elastic effects that were not considered in this work.

Two single fibre numerical models were tested under out-of-plane compression. Firstly, a homogenised where the fibre was modelled as a solid cylinder and secondly, a macro-fibril based where fibrillation was allowed to manifest through the cohesive contact definition. In Fig. 7a two strain hardening curves can be seen, one obtained from the experimental work in [6] and a modified which was proposed in this work. The latter was generated based on the numerical results of the homogenised model.

A comparison between the experimental and predicted out-of-plane compressive stress–strain behaviour, for the homogenised model, is presented in Fig. 7b. The numerical results, generated by using the experimentally obtained strain hardening curve, showed excellent correlation with the experimental stress–strain curve up to 30% nominal strain. At higher strains, the numerical response underpredicted the experimental and thus, the proposed strain hardening curve was used to amend for this discrepancy. The stress–strain response of the macro-fibril based model can be seen in 8c. The model showed good correlation up to 10% of nominal strain but experienced a more compliant behaviour at higher strains due to fibrillation. This could be expected since the hardening input curve from the experimental results in [6], included both geometrical and material non-linearities. In the macro-fibril based model, geometrical non-linearities were modelled explicitly by the cohesive contact failure which allowed the evolution of fibrillation.

Table 1
Constitutive model parameters.

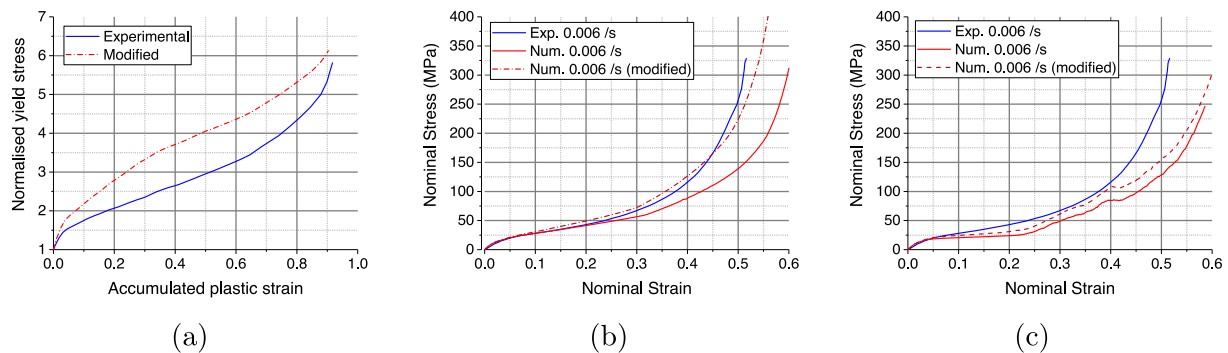| Dyneema® SK76 macro-fibril properties									
ρ (kg/m^3)	970	$\sigma_{y,22}$ (MPa)	20	p_1	0.19	τ_1 (s)	2.95e−5
E_{11} (GPa)	144.2	$\sigma_{y,33}$ (MPa)	20	p_2	0.11	τ_2 (s)	3.4
E_{22} (GPa)	2.87	$\sigma_{y,12}$ (MPa)	3.33	p_3	0.17	τ_3 (s)	77.9
E_{33} (GPa)	2.87	X_T (GPa)	4	p_4	0.17	τ_4 (s)	1725
G_{12} (GPa)	4.5	$\Gamma^T_{f_{11}}$ (kJ/m^2)	864	p_5	0.07	τ_5 (s)	5.93e5
G_{23} (GPa)	1.225			p_6	0.15	τ_6 (s)	3.11e7
G_{13} (GPa)	4						
ν_{12}	0.1						
ν_{23}	0.4						
ν_{13}	0.1						

(a)

(b)

(c)

Fig. 7. Single fibre experimental and numerical through-thickness compression results. (a) Strain hardening input curves; (b) Nominal stress–strain response (homogenised model); (c) Nominal stress–strain response (macro-fibril based model).

The deformed fibre cross-section of the macro-fibril based fibre models as well as the plastic strain distribution through-the-thickness can be seen in Fig. 8, for the value of 30% of nominal strain. The generated image were obtained using the proposed (modified) strain hardening master curve.

The out-of-plane compressive behaviour consisted of three regions. Firstly, the fibre showed an elastic response, followed by softening, fibrillation and accumulation of plastic strain until it finally reached a stiffening region [6]. The predicted yield stress was 12 MPa while the experimentally reported was 20 MPa. Fibrillation was initially observed from 1% to 26% of nominal strain followed by fibril compression and plastic strain accumulation up to 41% of nominal strain. Moreover, fibrillation propagated in the stiffening region (strain > 41%) where interfaces failed under shear and promoted macro-fibril sliding.

4.3. Thermoplastic polyurethane (TPU) resin characterisation

The resin was modelled with MAT24 which is a piecewise linear plasticity material model already available in LS-DYNA. Kinematic hardening was implemented using a master curve input for the yield stress of the resin over the accumulated plastic strain. Since the actual parameters of the PADP resin used in Dyneema® laminates were not available, experimental results for the Desmopan® 9665DU TPU resin were used for the validation of the model.

The tensile tests of the TPU were performed using a dogbone specimen type 1BA(BS ISO 527: 2012). Two strain rates were investigated, 100 mm/min and 600 mm/min. A comparison between the experimental and numerical results can be seen in Fig. 9.
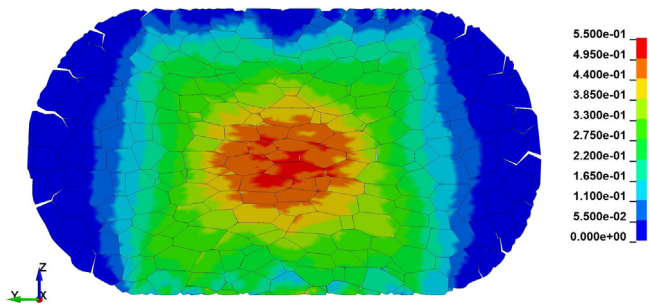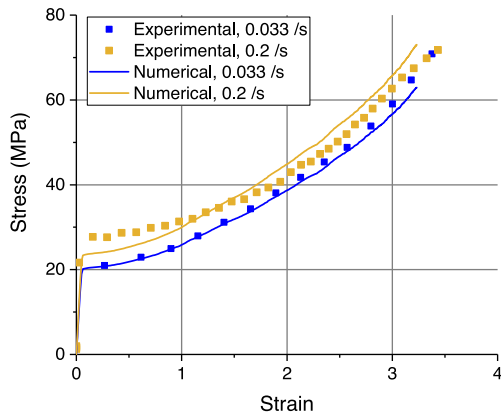
4.4. RVE results

4.4.1. In-plane tension

Four different strain-rates were studied for the RVE under in-plane tension. A comparison between the numerical results of this study and experimental results found in the literature can be seen in Fig. 10 and 11.

The numerical results from this study were able to capture the slope of the stress–strain curve that was observed in experimental results for various strain-rates. The average fibre volume fraction of the Dyneema® HB26 laminate is close to 83%, and thus small discrepancies were present due to the lower volume fraction of 80% in the model. The predicted strength from the FE models was 1.57 GPa, which is close to the theoretical value calculated by the following equation.

$$X_T \times V_f \times 0.5 \, ([0/90] \text{ configuration}) = 4\,\text{GPa} \times 80\% \times 0.5$$
$$= 1.6\,\text{GPa} \tag{20}$$

However, laminates contain yarns with multiple fibres that possess different values of strength due to manufacturing defects. When the macro-fibril strength was reduced to 3 GPa, which is the yarn's average strength [3], the predicted laminate strength was 1.18 GPa. A comparison between the predicted and experimentally obtained tensile strength from different studies can be seen in Table 2. A more appropriate way to predict the strength of the laminate would be to assign a different fibre strength in each element, following a statistical distribution.

It can be seen in Fig. 11, that other experimental studies [3], underpredict the strength of the laminate that was obtained by the DSM ply
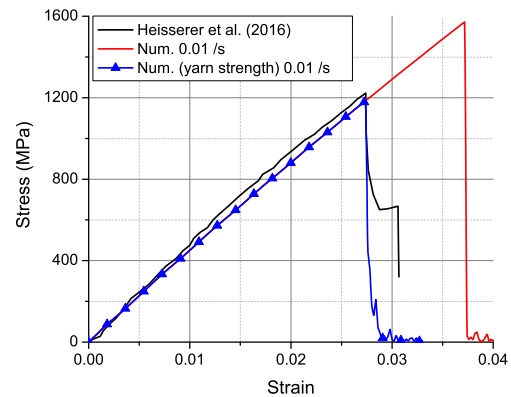

Fig. 8. Through-the-thickness macro-fibril plastic strain distribution, at 30% of nominal strain.

Fig. 10. Macro-fibril strength influence in the RVE tensile response.

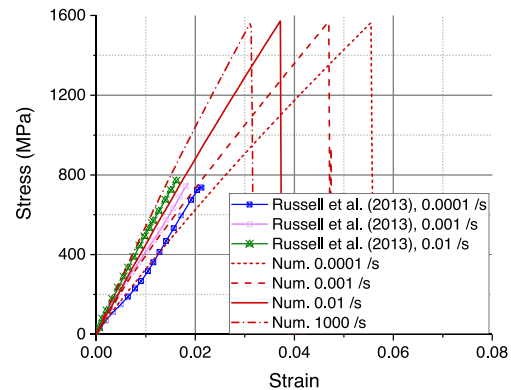**Fig. 9.** TPU tensile response.

Fig. 11. Experimental and RVE numerical tensile response under different strain rates.

Table 2
Numerical and experimental tenisle strength comparison.

Strain rate, $\dot{\varepsilon} = 0.01$ /s	DSM ply test [30]	Russell et al. [3]	RVE
Thickness (um)	270	6×10^3	35.2
Fibre Strength (GPa)	–	–	3
Laminate Strength (GPa)	1.22	0.77	1.18
Error %	3.27	34.7	–

tests [30]. By increasing the laminate thickness, the load cannot be transferred effectively from the outer layers to the core. A detailed sensitivity analysis on the coefficient of friction between the specimen and the grips for Dyneema® laminates, which underlines the aforementioned phenomenon, was presented by Iannucci et al. [12].

Contour maps of the contact nodal gap, in the 90 degree ply, can be seen in Fig. 12, in μm, for quasistatic 0.001/s, low 1/s and high 1000/s strain-rates. The images were taken at 3.24% of strain and fibrillation was observed under every strain-rates that was examined, with interface gaps varying from 0.2 to 2.2 nm.

The response of the resin was rate dependent and more compliant under quasistatic loading. As a results, the compressive force generated by the resin increased with the strain-rate and led to larger macro-fibril separation. The patterns of fibrillation were similar in both Fig. 12a and 12b, while the maximum magnitude of nodal gap increased in the latter. Under high strain-rates, Fig. 12c, the load could not be transferred effectively, from the resin to the fibre, hindering fibrillation. Macro-fibril to resin interface failure showed the same rate dependency as fibrillation with maximum values of 1.63, 1.78 and 0.13 nm for quasistatic, low and high strain-rates respectively. Lastly, none of the RVE models experienced complete interlaminar failure.

4.4.2. Out-of-plane compression

Results from the experimental work of Attwood et al. [11] were used to validate the behaviour of the RVE under out-of-plane compression. Larger width specimens, L = 7, 9 and 10 mm, were considered for validating the model since they were less affected by the free surfaces of the laminate. The model was subjected to a strain rate of 0.1/s. As seen in Fig. 13 the stress–strain response of the model over-predicted the one observed in the experiments for strains up to 15%.

The TPU resin used to make UHMWPE composites is usually porous and effects such as resin pore collapse and progressive fibre compaction are expected under compression. However, the pores were not explicitly modelled in this work and in order to assess the validity of the numerical model, the slope of the stress–strain curve needs to be studied.

A comparison between the stress–strain slopes is presented in Fig. 14. The predicted slope, showed a gradual increase at stresses higher than 200 MPa which is in accordance to the experimental
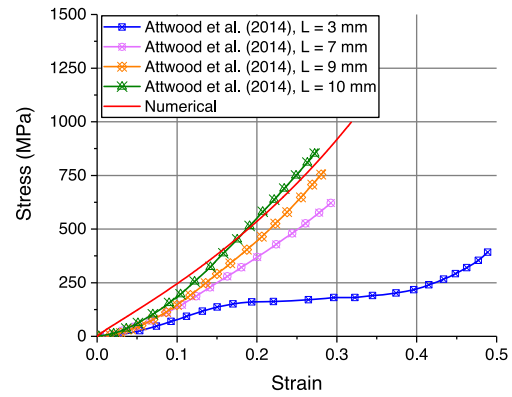

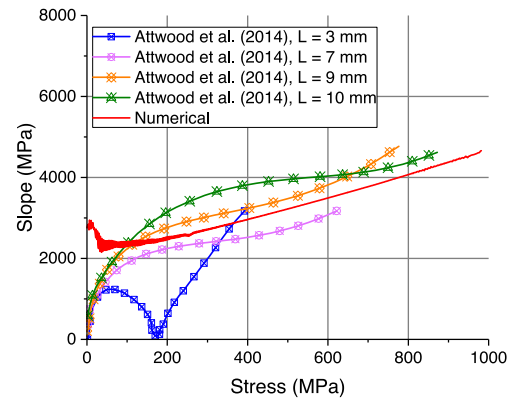**Fig. 13.** Experimental [11] and RVE numerical out-of-plane compression stress–strain results.

Fig. 14. Experimental [11] and RVE numerical out-of-plane compression stress–strain slope comparison.

observations. Numerical results were more compliant than the experimental curves for L = 9 and 10 mm, due to the lower fibre volume fraction in the model. Furthermore, only one fibre was modelled through the thickness of each ply which is not favourable for capturing the effects of fibre to fibre interaction. Fibre packing can be deemed important in accurately predicting the deformation and stress distribution in the micro-scale.

Periodic boundary conditions did not allow for excessive in-plane expansion, although they provided the expected deformation near the center of the specimen. Consequently, fibrillation was not observed as it is expected to develop under transverse fibre expansion which
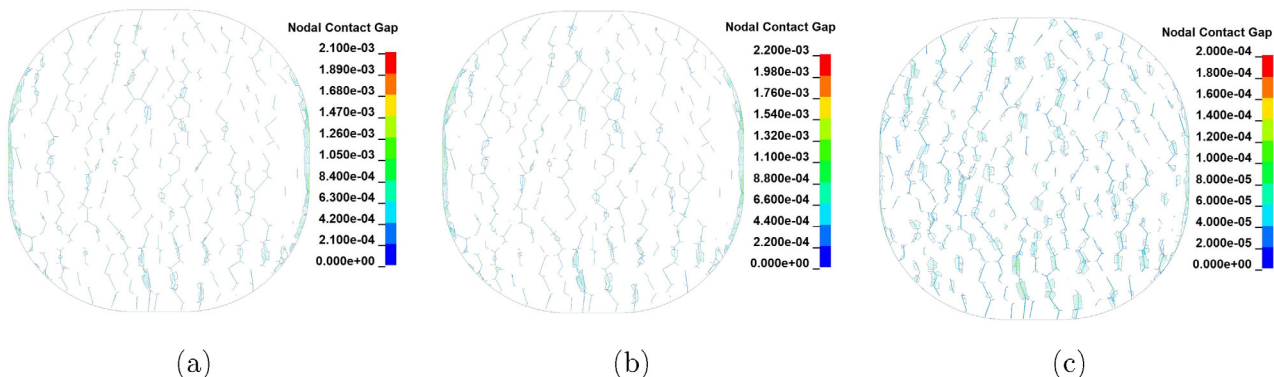

(a)　　　　　　　　(b)　　　　　　　　(c)

Fig. 12. Macro-fibril interface failure under tension at 3.24% of strain. Strain-rates: (a) $\dot{\varepsilon} = 0.001/s$; (b) $\dot{\varepsilon} = 1/s$; (c) $\dot{\varepsilon} = 1000/s$.

leads to macro-fibril interface failure. Furthermore, indirect tensile stresses, associated with the 0/90 ply orientation, were not significant enough to promote failure ply rupture.

The distribution of the plastic strain through the thickness is presented in Fig. 15 at 20% of macroscopic strain. Maximum plastic strain values were observed near the center of each fibre.

4.4.3. In-plane shear

The response of the RVE under in-plane shear loading was tested, at a strain-rate of 0.014/s, and compared to experimental results found in the literature [10]. As seen in Fig. 16, the macro-fibril based model followed accurately the non-linear trend observed in the experiments but overpredicted the stress. The RVE enters the stiffening region prematurely and fracture can be promoted only by macro-fibril tensile failure. The RVE in-plane shear strength was directly related to the macro-fibril tensile strength and higher than the experimentally obtained value. A failure criterion for the resin is needed for the accurate laminate strength prediction under in-plane shear.

The stress–strain response is highly dependent on the resin properties and thus discrepancies were introduced due to the difference between the properties of the actual PADP resin used to manufacture the laminates and the properties used in the model. Moreover, the shear response of the macro-fibril was predicted according to Hill's yield criterion and the in-plane shear yield strength was assumed to be $\sqrt{36}$ times lower than the one measured in the transverse direction of the fibre, according the work in [31]. To the best of the author's knowledge, the actual in-plane shear behaviour has not been measured for the fibre and a decoupled yield criterion might be more appropriate to express the shear response of the macro-fibril.

Experimental results in Fig. 16 were obtained by in-plane tension-shear tests according to BS EN ISO 14129:1998 [32]. Micromechanical modelling is generally focused on a point inside the laminate while the actual specimen experiences local stress concentration near the tabs, as seen in Fig. 17. This effect was also expected to hinder the correlation between the predicted and experimentally measured mechanical behaviour.

The distribution of the plastic in-plane shear strain in the macro-fibrils is presented in Fig. 18 at $\gamma_{xy} = 0.41$. The distribution is heterogeneous through the thickness of the RVE which indicates interfaces failure, allowing macro-fibrils to move independently from each other. Macro-fibril sliding was observed with the maximum relative nodal displacement, being close to the center of the fibre. The measured values were 82, 307, 479 and 719 nm at $\gamma_{xy} = 0.46, 0.81, 0.86$ and 0.87 respectively.
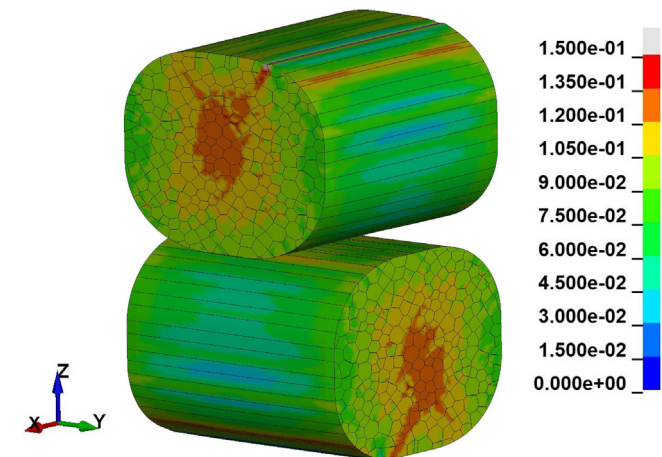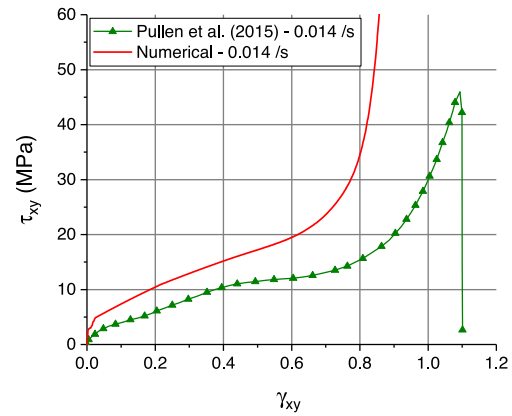
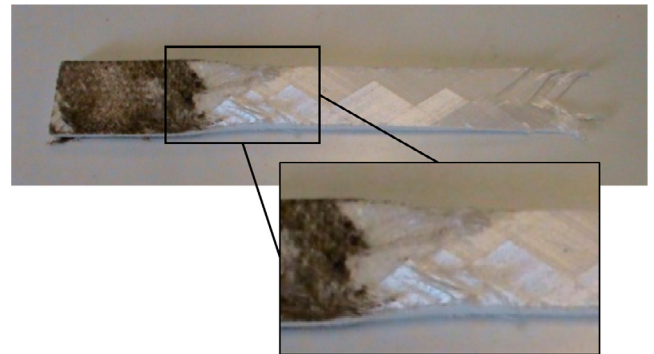**Fig. 16.** Experimental [10] and RVE numerical in-plane shear stress–strain response.

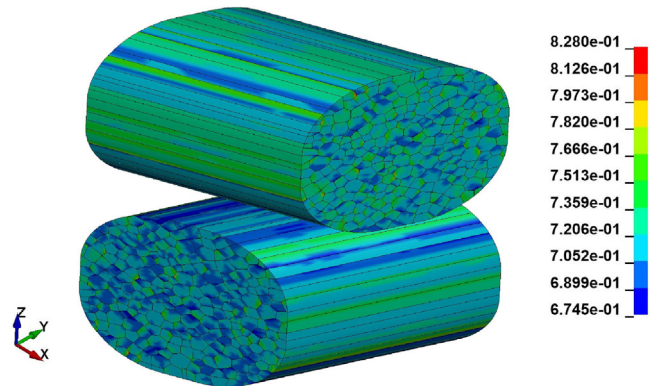**Fig. 17.** Failed tension-shear specimen (250 mm × 25 mm) [33].

Fig. 18. In-plane plastic shear strain distribution at $\gamma_{xy} = 0.41$.

Debonding between the macro-fibrils and the resin was observed in small regions, scattered around the perimeter of the fibre, allowing the cohesive interaction to stay in effect throughout the analysis. The RVE fully delaminated at $\gamma_{xy} = 0.52$ where the stress–strain curve entered the convex stiffening region.

5. Discussion and conclusion

A RVE model for UHWMPE composites was developed and validated under tensile, compressive and shear loading conditions. The fibre consisted of continuous macro-fibrils through its length, which made it possible for fibrillation to manifest. A user defined constitutive model was developed to account for the non-linear and time depen-

Fig. 15. Through-thickness macro-fibril plastic strain distribution at 20% of macroscopic strain.

dent behaviour of the fibre. The proposed constitutive model was able to capture accurately the phenomena observed in the experiments. The macro-fibril based, single fibre, numerical model showed a more compliant behaviour than the one obtained from experiments, under through thickness compression. This observation along with the under predicted yield stress suggests that a modified strain hardening curve is needed. A direct optimisation on the experimentally obtained stress–strain curve using the macro-fibril based model is subject to future work.

Various strain-rates ranging from 10^{-4} to $1000/s$ were examined under in-plane tension. The viscoelastic model was able to capture the rate dependency observed in the experiments. Fibrillation and fibril-resin interface failure were driven by the resin's response and thus, showed rate dependency. Maximum separation was observed at low strain-rates followed by quasistatic and lastly high strain-rates.

The implementation of a strain-rate and pressure dependent cohesive contact interaction is expected to provide a more accurate insight in interface failure phenomena, especially under high loading rates. Moreover, a statistical variation of the macro-fibril strength is believed to be of high significance and needs to be considered for accurate laminate strength predictions.

Both the through-thickness compression stress–strain curve and slope were in good agreement with the experimental results. Plastic strain in the fibre developed mostly in the centre and fibrillation was not observed due to the lack of in-plane expansion in the model.

The RVE was able to predict the non-linear, in-plane shear, stress––strain curve trend, that was observed in the tests. The manufacturing process may introduce residual thermal strains, which could be included in the future along with the properties of the actual resin used in Dyneema® HB26, both of which are expected improve the accuracy of the numerical model. Furthermore, single fibre pull-out tests could provide useful information on the fibre/resin interface properties. The applicability of a decoupled yield criterion remains under investigation as it could improve the accuracy of the numerical model under in-plane shear.

Finally, the porosity in the resin needs to be modelled explicitly as it is expected to affect the load transferring efficiency to the fibres and show how deformation evolves in the RVE when the strain is being localised around the pores. This would also prove beneficial for the prediction of shear strength as failure is expected to initiate around the largest flaws in the resin.

CRediT authorship contribution statement

D. Kempesis: Conceptualization, Methodology, Software, Validation, Investigation, Writing - original draft, Visualization. **L. Iannucci:** Project administration, Funding acquisition, Supervision, Conceptualization, Methodology, Resources, Writing - review & editing, Investigation. **S. Del Rosso:** Supervision, Investigation, Writing - review & editing. **P.T. Curtis:** Conceptualization, Writing - review & editing. **D. Pope:** Conceptualization, Writing - review & editing. **P.W. Duke:** Project administration, Conceptualization, Writing - review & editing.

Declaration of Competing Interest

The authors declare that they have no known competing financial interests or personal relationships that could have appeared to influence the work reported in this paper.

Acknowledgement

Appendix A. Recursive algorithm

Stress as a function of strain and time:

$$\sigma(t) = \int_0^t E(t-\tau)\dot{\varepsilon}(\tau)d\tau \tag{A.1}$$

Change of stiffness over time (Prony series):

$$E(t) = E_0\left[1 - \sum_{k=1}^6 p_k\left(1 - e^{\frac{-t}{\tau_k}}\right)\right] = E_\infty + E_0\sum_{k=1}^6 p_k e^{\frac{-t}{\tau_k}} \Rightarrow E(t)$$

$$= E_\infty + \sum_{k=1}^6 E_k e^{\frac{-t}{\tau_k}} \tag{A.2}$$

where E_∞ is the elastic response when the viscoelastic terms are fully relaxed and E_k the instantaneous stiffness of each viscoelastic term. From A.1 and A.2:

$$\sigma(t) = \int_0^t E_\infty \dot{\varepsilon}(\tau)d\tau + \int_0^t \sum_{k=1}^6 E_k e^{\frac{-(t-\tau_k)}{\tau_k}}\dot{\varepsilon}(\tau)d\tau =$$

$$= E_\infty \int_0^t \dot{\varepsilon}(\tau)d\tau + \sum_{k=1}^6 E_k \int_0^t e^{\frac{-(t-\tau)}{\tau_k}}\dot{\varepsilon}(\tau)d\tau \Rightarrow \sigma(t)$$

$$= \sigma^{el} + \sum_{k=1}^6 E_k I_k \tag{A.3}$$

The viscous strain at the end of the increment can be calculated:

$$I_k^{n+1} = \int_0^t e^{\frac{-(t_{n+1}-\tau)}{\tau_k}}\dot{\varepsilon}(\tau)d\tau =$$

$$= \int_0^{t_n} e^{\frac{-(t_{n+1}-\tau)}{\tau_k}}\dot{\varepsilon}(\tau)d\tau + \int_{t_n}^{t_{n+1}} e^{\frac{-(t_{n+1}-\tau)}{\tau_k}}\dot{\varepsilon}(\tau)d\tau \tag{A.4}$$

where $\Delta t = t_{n+1} - t_n$

$$e^{\frac{-(t_{n+1}-\tau_k)}{\tau_k}} = e^{\frac{-(t_n+\Delta t-\tau)}{\tau_k}} = e^{\frac{-\Delta t}{\tau_k}}e^{\frac{-(t_n-\tau)}{\tau_k}} \tag{A.5}$$

The strain-rate $\dot{\varepsilon}(\tau)$ can be assumed to stay constant over a time increment between n and $n+1$.

$$\therefore I_k^{n+1} = e^{\frac{-\Delta t}{\tau_k}}\int_0^{t_n} e^{\frac{-(t_n-\tau)}{\tau_k}}\dot{\varepsilon}(\tau)d\tau + \int_{t_n}^{t_{n+1}} e^{\frac{-\Delta t}{\tau_k}}e^{\frac{-(t_n-\tau)}{\tau_k}}\dot{\varepsilon}(\tau)d\tau \Rightarrow I_k^{n+1}$$

$$= e^{\frac{-\Delta t}{\tau_k}}I_k^n + \left(1 - e^{\frac{-\Delta t}{\tau_k}}\right)\tau_k\dot{\varepsilon}(\tau) \tag{A.6}$$

Appendix B. Return mapping algorithm

The following algorithm was used to update the stress in the plastic region, according to [15]. The stress can be expressed as a function of the plastic multiplier $\Delta\gamma$ which is used to return the stress on the yield surface defined by the ($\overline{\sigma}$ - $\overline{\varepsilon}_p$) master curve. The yield function can be expressed in the following form:

$$\Phi = \frac{1}{2}\boldsymbol{\sigma}^\top\boldsymbol{P}\boldsymbol{\sigma} - \left[\overline{\sigma}(\overline{\varepsilon}_p)\right]^2 \tag{B.1}$$

An initial guess for the scalar plastic multiplier $\Delta\gamma$ is used to begin the calculation. The stress can be written as a function of $\Delta\gamma$.

$$\boldsymbol{\sigma}(\Delta\gamma)^{n+1} = (\boldsymbol{I} + \Delta\gamma\boldsymbol{CP})^{-1}\boldsymbol{\sigma}^{trial} \tag{B.2}$$

where $\boldsymbol{I}$ is the identity matrix. The plastic flow rate tensor is given below:

$$\dot{\boldsymbol{\varepsilon}}_p = \dot{\gamma}\boldsymbol{P}\boldsymbol{\sigma} \tag{B.3}$$

The Newton–Raphson method was employed to solve Eq. B.4.

$$\Phi(\Delta\gamma) = \frac{1}{2}\boldsymbol{\sigma}(\Delta\gamma)^\top\boldsymbol{P}\boldsymbol{\sigma}(\Delta\gamma) - \left[\overline{\sigma}(\overline{\varepsilon}_p(\Delta\gamma))\right]^2 \tag{B.4}$$

The derivative of the yield function is given below:

$$\frac{d\Phi(\Delta\gamma)}{d\Delta\gamma} = (\boldsymbol{P}\boldsymbol{\sigma}(\Delta\gamma))^{\intercal}\frac{d\boldsymbol{\sigma}}{d\Delta\gamma} - 2\overline{\sigma}(\Delta\gamma)\overline{H}\frac{d\overline{\varepsilon}_p}{d\Delta\gamma} \tag{B.5}$$

where $\overline{H}$ is the slope of the non-dimensional hardening curve input.

$$\overline{H} = \frac{d\overline{\sigma}}{d\overline{\varepsilon}_p} \tag{B.6}$$

The plastic multiplier is updated as follows:

$$\delta\Delta\gamma^n = -\frac{\Phi(\Delta\gamma)}{\frac{d\Phi(\Delta\gamma)}{d\Delta\gamma}} \tag{B.7}$$

$$\Delta\gamma^{n+1} = \Delta\gamma^n + \delta\Delta\gamma^n \tag{B.8}$$

The derivatives of the stress and accumulated plastic strain with respect to the plastic multiplier are given by the following expressions:

$$\frac{d\boldsymbol{\sigma}}{d\Delta\gamma} = -(\boldsymbol{I} + \Delta\gamma\boldsymbol{CP})^{-1}\boldsymbol{CP}\boldsymbol{\sigma}(\Delta\gamma) \tag{B.9}$$

$$\frac{d\overline{\varepsilon}_p}{d\Delta\gamma} = \sqrt{\frac{2}{3}(\boldsymbol{P}\boldsymbol{\sigma}(\Delta\gamma))^{\intercal}\boldsymbol{Z}\boldsymbol{P}\boldsymbol{\sigma}(\Delta\gamma)} \tag{B.10}$$

Finally, the stress and the accumulated plastic strain can be calculated as follows:

$$\boldsymbol{\sigma}(\Delta\gamma)^{n+1} = \boldsymbol{\sigma}(\Delta\gamma)^n - \delta\Delta\gamma\left[(\boldsymbol{I} + \Delta\gamma\boldsymbol{CP})^{-1}\boldsymbol{CP}\boldsymbol{\sigma}(\Delta\gamma)^n\right] \tag{B.11}$$

$$\overline{\varepsilon}_p^{n+1}(\Delta\gamma) = \overline{\varepsilon}_p^n(\Delta\gamma) + \Delta\gamma\sqrt{\frac{2}{3}(\boldsymbol{P}\boldsymbol{\sigma}(\Delta\gamma))^{\intercal}\boldsymbol{Z}\boldsymbol{P}\boldsymbol{\sigma}(\Delta\gamma)} \tag{B.12}$$

The symmetric stiffness matrix $\boldsymbol{C}$:

$$\boldsymbol{C} = \begin{bmatrix} C_{11} & C_{12} & C_{13} & 0 & 0 & 0 \\ C_{12} & C_{22} & C_{23} & 0 & 0 & 0 \\ C_{13} & C_{23} & C_{33} & 0 & 0 & 0 \\ 0 & 0 & 0 & C_{44} & 0 & 0 \\ 0 & 0 & 0 & 0 & C_{55} & 0 \\ 0 & 0 & 0 & 0 & 0 & C_{66} \end{bmatrix} \tag{B.13}$$

where the coefficients are given by:

$$\begin{aligned} & C_{11} = \frac{(1-\nu_{23}\nu_{32})E_{11}}{\Omega}, \quad C_{12} = \frac{(\nu_{21}+\nu_{31}\nu_{23})E_{11}}{\Omega} \\ & C_{22} = \frac{(1-\nu_{13}\nu_{31})E_{22}}{\Omega}, \quad C_{23} = \frac{(\nu_{32}+\nu_{12}\nu_{31})E_{22}}{\Omega} \\ & C_{33} = \frac{(1-\nu_{12}\nu_{21})E_{33}}{\Omega}, \quad C_{13} = \frac{(\nu_{31}+\nu_{21}\nu_{23})E_{11}}{\Omega} \\ & C_{44} = G_{12}, \quad C_{55} = G_{23}, \quad C_{66} = G_{13} \\ & \Omega = 1 - \nu_{12}\nu_{21} - \nu_{23}\nu_{32} - \nu_{13}\nu_{31} - 2\nu_{21}\nu_{32}\nu_{13} \\ & \frac{\nu_{ij}}{E_{ii}} = \frac{\nu_{ji}}{E_{jj}}, \quad (\text{for}\, i, j = 1, 2, 3) \end{aligned} \tag{B.14}$$

The matrix $\boldsymbol{P}$ includes the parameters of the yield function and is given as:

$$\boldsymbol{P} = 2\begin{bmatrix} F_1+F_3 & -F_1 & -F_3 & 0 & 0 & 0 \\ -F_1 & F_1+F_2 & -F_2 & 0 & 0 & 0 \\ -F_3 & -F_2 & F_2+F_3 & 0 & 0 & 0 \\ 0 & 0 & 0 & F_4 & 0 & 0 \\ 0 & 0 & 0 & 0 & F_5 & 0 \\ 0 & 0 & 0 & 0 & 0 & F_6 \end{bmatrix} \tag{B.15}$$

$$\boldsymbol{Z} = \begin{bmatrix} 1 & 0 & 0 & 0 & 0 & 0 \\ 0 & 1 & 0 & 0 & 0 & 0 \\ 0 & 0 & 1 & 0 & 0 & 0 \\ 0 & 0 & 0 & \frac{1}{2} & 0 & 0 \\ 0 & 0 & 0 & 0 & \frac{1}{2} & 0 \\ 0 & 0 & 0 & 0 & 0 & \frac{1}{2} \end{bmatrix} \tag{B.16}$$

References

[1] Marissen R. Design with ultra strong polyethylene fibers. Mater Sci Appl 2011;02 (05):319–30. https://doi.org/10.4236/msa.2011.25042.

[2] Strawhecker KE, Sandoz-Rosado EJ, Stockdale TA, Laird ED. Interior morphology of high-performance polyethylene fibers revealed by modulus mapping. Polymer 2016;103:224–32. https://doi.org/10.1016/j.polymer.2016.09.062.

[3] Russell BP, Karthikeyan K, Deshpande VS, Fleck NA. The high strain rate response of ultra high molecular-weight polyethylene: from fibre to laminate. Int J Impact Eng 2013;60:1–9. https://doi.org/10.1016/j.ijimpeng.2013.03.010.

[4] Kromm FX, Lorriot T, Coutand B, Harry R, Quenisset JM. Tensile and creep properties of ultra high molecular weight PE fibres. Polym Test 2003;22 (4):463–70. https://doi.org/10.1016/S0142-9418(02)00127-7.

[5] Sanborn B, DiLeonardi AM, Weerasooriya T. Tensile properties of Dyneema SK76 single fibers at multiple loading rates using a direct gripping method. J Dyn Behav Mater 2015;1(1):4–14. https://doi.org/10.1007/s40870-014-0001-3.

[6] Sockalingam S, Casem D, Weerasooriya T, McDaniel P, Gillespie J. Experimental investigation of the high strain rate transverse compression behavior of ballistic single fibers. J Dyn Behav Mater 2017;3(3):474–84. https://doi.org/10.1007/s40870-017-0126-2.

[7] Meshi I, Levi-Sasson A, Breiman U, Haj-Ali R. The parametric HFGMC micromechanical model for soft UHMWPE laminated composites. Mech Mater 2020;141:. https://doi.org/10.1016/j.mechmat.2019.103223 103223.

[8] Grujicic M, Arakere G, He T, Bell WC, Cheeseman BA, Yen CF, Scott B. A ballistic material model for cross-plied unidirectional ultra-high molecular-weight polyethylene fiber-reinforced armor-grade composites. Mater Sci Eng A 2008;498(1–2):231–41. https://doi.org/10.1016/j.msea.2008.07.056.

[9] Xia Z, Chen Y, Ellyin F. A meso/micro-mechanical model for damage progression in glass-fiber/epoxy cross-ply laminates by finite-element analysis. Compos Sci Technol 2000;60(8):1171–9. https://doi.org/10.1016/S0266-3538(00)00022-1.

[10] Pullen AD, Louca LA, Micallef K, Soleiman Fallah A, Curtis PT. Characterization of the mechanical behavior of a polymer-based laminate and constituent fibers at various quasi-static strain rates. J Aerosp Eng 28 (5). doi:10.1061/(ASCE)AS.1943-5525.0000460..

[11] Attwood JP, Khaderi SN, Karthikeyan K, Fleck NA, Omasta MR, Wadley HNG, Deshpande VS. The out-of-plane compressive response of Dyneema composites. J Mech Phys Solids 2014;70(1):200–26. https://doi.org/10.1016/j.jmps.2014.05.017.

[12] Iannucci L, Del Rosso S, Curtis PT, Pope DJ, Duke PW. Understanding the thickness effect on the tensile strength property of Dyneema HB26 laminates. Materials 11 (8). doi:10.3390/ma11081431..

[13] Hallquist J. LS-DYNATheory manual. Livermore Software Technology Corporation (LSTC)..

[14] Livermore Software Technology Corporation (LSTC), LS-DYNA Keyowrd User's Manual, R9.0, vol. II..

[15] de Souza Neto EA, Peric D, Owen DRJ. Computational methods for plasticity: theory and application. John Wiley & Sons; 2011.

[16] Bažant ZP, Oh BH. Crack band theory for fracture of concrete. Matér Constr 1983;16(3):155–77. https://doi.org/10.1007/BF02486267.

[17] Iannucci L, Ankersen J. An energy based damage model for thin laminated composites. Compos Sci Technol 2006;66(7–8):934–51. https://doi.org/10.1016/j.compscitech.2005.07.033.

[18] Oliver J. A consistent characteristic length for smeared cracking models. Int J Numer Methods Eng 1989;28:461–74. https://doi.org/10.1002/nme.1620280214.

[19] Donadon MV, Iannucci L, Falzon BG, Hodgkinson JM, de Almeida SFM. A progressive failure model for composite laminates subjected to low velocity impact damage. Comput Struct 2008;86(11–12):1232–52. https://doi.org/10.1016/j.compstruc.2007.11.004.

[20] McDaniel PB, Deitzel JM, Gillespie JW. Structural hierarchy and surface morphology of highly drawn ultra high molecular weight polyethylene fibers studied by atomic force microscopy and wide angle X-ray diffraction. Polymer 2015;69:148–58. https://doi.org/10.1016/j.polymer.2015.05.010.

[21] Falco S, Jiang J, De Cola F, Petrinic N. Generation of 3D polycrystalline microstructures with a conditioned Laguerre-Voronoi tessellation technique. Comput Mater Sci 2017;136:20–8. https://doi.org/10.1016/j.commatsci.2017.04.018.

[22] McDaniel PB, Deitzel JM, Gregory D, Polakovic T, Gillespie JW. Single fiber peel test to assess ultra high molecular weight polyethylene fiber mesostructure interactions. J Appl Polym Sci 2018;135(16):1–11. https://doi.org/10.1002/app.46156.

[23] Staniszewski JM, Sockalingam S, Bogetti TA, Gillespie JW. Modeling the fibrillation of Kevlar KM2 single fibers subjected to transverse compression. Fibers Polym 2018;19(7):1479–89. https://doi.org/10.1007/s12221-018-8127-x.

[24] Singletary J, Davis H, Ramasubramanian MK, Knoff W, Toney M. Transverse compression of PPTA fibers. Part I. Single fiber transverse compression testing. J Mater Sci 2000;35(3):573–81. https://doi.org/10.1023/A:1004764024568.

[25] Turon A, Dávila CG, Camanho PP, Costa J. An engineering solution for mesh size effects in the simulation of delamination using cohesive zone models. Eng Fract Mech 2007;74(10):1665–82. https://doi.org/10.1016/j.engfracmech.2006.08.025.

[26] Garoz D, Gilabert FA, Sevenois RD, Spronk SW, Van Paepegem W. Consistent application of periodic boundary conditions in implicit and explicit finite element simulations of damage in composites. Compos B Eng 168 (November 2018): 2019; 254–266. doi:10.1016/j.compositesb.2018.12.023..

[27] Lässig T, Nguyen L, May M, Riedel W, Heisserer U, Van Der Werff H, Hiermaier S. A non-linear orthotropic hydrocode model for ultra-high molecular weight polyethylene in impact simulations. Int J Impact Eng 2015;75(10):110–22. https://doi.org/10.1016/j.ijimpeng.2014.07.004.

[28] Grujicic M, Glomski PS, He T, Arakere G, Bell WC, Cheeseman BA. Material modeling and ballistic-resistance analysis of armor-grade composites reinforced with high-performance fibers. J Mater Eng Perf 2009;18(9):1169–82. https://doi.org/10.1007/s11665-009-9370-5.

[29] Del Rosso S. Micro-scale Hybrid Fbres for Low Cost Polymer Armours. Imperial College London; 2014. https://doi.org/10.25560/50702.

[30] Heisserer U, can der Werff H. Which strength of dyneema fiber composites to use in hydrocode models? In: Proceedings of the 29th international symposium on ballistics (ISB); 2016..

[31] Sockalingam S, Bremble R, Gillespie JW, Keefe M. Transverse compression behavior of Kevlar KM2 single fiber. Compos A Appl Sci Manuf 2016;81:271–81. https://doi.org/10.1016/j.compositesa.2015.11.032.

[32] British Standards Institution (BSI), Fibre-reinforced plastic composites. determination of the in-plane shear stress/shear strain response, including the in-plane shear modulus and strength by the ±45) tension test method. BS EN ISO 14129; 1998..

[33] Iannucci L, Pope D. High velocity impact and armour design. Express Polym Lett 2011;5(3):262–72. https://doi.org/10.3144/expresspolymlett.2011.26.